PCCP

PAPER

View Article Online
View Journal | View Issue

Cite this: *Phys. Chem. Chem. Phys.*, 2025, **27**, 18141

Resonance charge exchange and collision integrals for $O(^3P)$–$O^+(^4S)$ and $O(^1D)$–$O^+(^4S)$ interactions

Zi Ding and Linhua Liu *

Received 31st March 2025,
Accepted 26th July 2025

DOI: 10.1039/d5cp01234a

rsc.li/pccp

Oxygen atom (O) collision with oxygen ions (O^+) plays a crucial role in air plasma systems. This work presents a theoretical study of inelastic (resonance charge transfer), elastic, and total collision integrals for $O(^3P)$–$O^+(^4S)$ and $O(^1D)$–$O^+(^4S)$ interactions in the temperature range of 500–50 000 K. The calculation is performed using the semi-classical method, based on the high-level potential energy curves obtained by the state-of-the-art *ab initio* method. The resonance charge exchange cross sections are in good agreement with those experiment values. The contributions of elastic and inelastic collision processes to the diffusion collision integrals are quantitatively estimated. The calculated collision data can be used to support the simulation of high-temperature air plasmas.

1. Introduction

Collisions between atoms and ions play a critical role in many non-equilibrium plasma systems, such as the electric-arc positive column,[1] re-entry vehicle analysis,[2,3] the design of aerospace vehicles operating at high-temperatures,[4] and the planet's thermosphere and ionosphere studies.[5] At temperatures sufficient to completely dissociate and partially ionize air, the thermal conductivity of air is largely determined by the atom–ion collision process, since the main mechanism of heat conduction under these conditions is the diffusion transfer of the enthalpy of ionization.[6] For homonuclear atom–parent–ion collisions, the resonance charge exchange process[7,8] greatly increases the diffusion cross sections by converting the scintillation collision between ions and atoms into a distinct head-on collision.[6,9,10] To accurately determine the transport properties of air plasmas, it is important to study homonuclear atom–ion interactions (N–N^+ and O–O^+ interactions). The authors have conducted a detailed study of collisions in N–N^+ interactions,[11] and this work will focus on O–O^+ collision processes, providing *ab initio*-derived collision data to bridge critical gaps in air plasma modeling.

According to Chapman–Enskog theory,[12,13] the transport coefficients (diffusivity, viscosity, and thermal conductivity) can be expressed as linear combinations of the collision integrals (cross sections).[14,15] Over the past few decades, considerable studies have focused on the collision of O–O^+ interactions. Konf *et al.*[6] evaluated resonance charge exchange cross sections from 0.1 to 10 000 eV using the Hulburt–Hirschfelder (HH) potentials. Levin and Wright[16] applied the Tang–Toennies potential to compute diffusion and viscosity-type collision integrals for $O^+(^4S)$–$O(^3P)$ interactions in the temperature range of 300–12 000 K. Similarly, Capitelli *et al.*[17] calculated diffusion and viscosity collision integrals of $O^+(^4S)$–$O(^3P)$ interactions based on the analytical potentials. Stallcop *et al.*[18] employed quantum mechanical methods with Wentzel–Kramers–Brillouin (WKB) approximations to calculate the transport cross sections for the $O^+(^4S)$–$O(^3P)$ interaction, providing collision integrals for temperatures ranging from 250 to 10 000 K. They used a complete active space self-consistent-field (CASSCF) method to obtain the potential energy curves (PECs), and refine using measured data. Additionally, Laricchiuta *et al.*[19] provided the inelastic, elastic, and total collision integrals for $O(^3P, {}^1D, {}^1S)$–$O^+(^4S, {}^2D, {}^2P)$ interactions based on the Morse and repulsive potentials.

Despite these contributions, earlier studies still exhibit two main limitations. First, the precision of the PECs directly impacts the reliability of transport property predictions.[11] Many studies have emphasized that the quality of PECs significantly affects collision integrals.[11,20–22] For example, Buchowiecki *et al.*[22] pointed out that *ab initio*-based collision integrals can deviate by over 10% from those of analytical functions at low temperatures. It is noted that only the results of Stallcop *et al.*[18] were calculated by the *ab initio* method. Most previous studies often relied on simplified analytical potentials (*e.g.* Morse, Tang–Toennies, HH, and repulsive potentials), which may lack the precision required for modern applications. In recent years, *ab initio* quantum chemistry has become a reliable method for generating high-precision potential energy data.[23] Some recent

School of Nuclear Science, Energy and Power Engineering, Shandong University, Jinan 250061, China. E-mail: liulinhua@sdu.edu.cn

studies preferred to use *ab initio* methods to determine the collision integrals when it is possible.[2,3] Second, most earlier studies have focused exclusively on collisions between ground-state $O^+(^4S)$ and $O(^3P)$ atoms. However, excited states play a substantial role in transport properties under high-temperature conditions, especially for the first excited state.[11,21,24,25] To date, only Laricchiuta *et al.*[19] explored the excited states for O–O^+ interactions using the Morse and repulsive potentials. While their analysis provides a comprehensive exploration, the derived data may not fully encompass the temperature range essential for spacecraft design, and the reliance on analytic approximations could introduce uncertainties in accuracy. Thus, it is necessary to conduct *ab initio* collision studies for O–O^+ interactions including ground state and excited state interactions.

Here, we calculate high-quality potential energy points for $O(^3P)$–$O^+(^4S)$ and $O(^1D)$–$O^+(^4S)$ interactions using multireference configuration interaction methods with the Davidson correction (icMRCI + Q) methods with Hartree–Fork (HF) and the CASSCF techniques. Specifically, the calculated potential energy points cover a wide range including the short-range region to ensure the accuracy of transport data. Subsequently, we calculate the elastic and inelastic transport collision cross sections, and provide inelastic, elastic and total collision integrals in the temperature range of 500 to 50 000 K.

The structure of the present paper is as follows. Section 2 presents the methodology of collision integrals, the details of our *ab initio* calculations, and the determination of collision pairs. Section 3 gives and discusses the contribution of elastic and inelastic collisions for cross sections and collision integrals. Finally, a summary of work and future perspectives is given in Section 4.

2. Theory

Despite significant advancements in computational technology, the computational resources required to simulate all possible collision pairs using *ab initio* methods to determine transport coefficients of high-temperature air plasma are still prohibitive. To balance computational efficiency with accuracy, identifying dominant collision pairs is essential. Considering the energy levels of O and O^+, the dominant collision pair can be determined by the population distribution of O. Assume that the O and O^+ in the plasma mixture are in thermodynamic equilibrium below 30 000 K, with only the states $O^+(^4S)$, $O(^3P)$, $O(^1D)$, and $O(^1S)$ are considered, and their populations in the ground and excited states satisfy the Boltzmann distribution equation. According to the Boltzmann distribution equation, the population distribution of oxygen atoms across electronic energy states under thermal equilibrium can be expressed as[21]

$$\frac{n_j}{n_i} = \frac{g_j}{g_i}\exp\left(-\frac{\Delta E_{ij}}{k_B T}\right) \tag{1}$$

where n represents the equilibrium population of the ith electronic level of a particle, the statistical weight g_i is the degeneracy of the energy level, and ΔE_{ij} is the energy difference between the ith energy level and jth energy level atomic oxygen. Fig. 1 shows the proportion of the first four excited electronic states of oxygen to the total number of O atoms. The first two electronic states of oxygen ($O(^3P)$ and $O(^1D)$) dominate the population distribution, accounting for nearly 99% of total O atoms below 20 000 K. Even at 50 000 K, the contribution of the second excited states is still small, accounting for only ~3%. Consequently, this work focuses on the collision processes of $O(^3P)$–$O^+(^4S)$ and $O(^1D)$–$O^+(^4S)$ interactions.

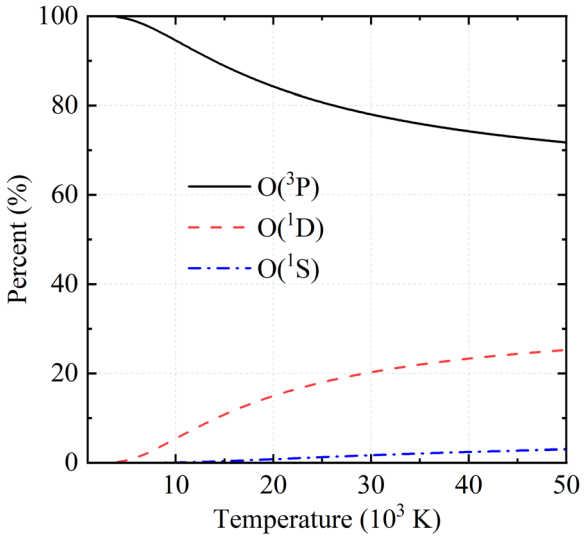

Fig. 1 The percentage of oxygen atoms in the first three electron states, where the solid line is the ground state, the dashed line is the first excited state, and the dot line is the second excited state.

According to the Chapman–Enskog method,[12,13] the average reduced collision integrals can be written as

$$\sigma^2\Omega^{(n,s)*} = \frac{F(n,s)}{2(k_B T)^{s+2}}\int_0^\infty e^{-E/(k_B T)} E^{s+1}\bar{Q}^n(E)\mathrm{d}E \tag{2}$$

where (n, s) is the order of the collision integral, E is the collision energy, k_B is the Boltzmann constant, T is the temperature, and $\bar{Q}^n$ is the mean transport cross sections, and the scale factor $F(n, s)$ can be expressed as[26]

$$F(n,s) = \frac{4(n+1)}{\pi(s+1)![2n+1-(-1)^n]} \tag{3}$$

For the atom–parent–ion interactions, total collision integrals should include the contribution of inelastic and elastic collisions,[27]

$$\sigma^2\Omega^{(n,s)*}_{\text{total}} = \sqrt{\left(\sigma^2\Omega^{(n,s)*}_{\text{in}}\right)^2 + \left(\sigma^2\Omega^{(n,s)*}_{\text{el}}\right)^2} \tag{4}$$

where the subscripts in and el represent the collision integrals of inelastic and elastic collisions, respectively. Within the framework of quantum scattering theory, the cross section for the resonance charge exchange is expressed in terms of the scattering phase shifts η_l, which depend solely on the PECs of

Table 1 The weighting factors for the calculation of cross sections

$O(^3P)$–$O^+(^4S)$		$O(^1D)$–$O^+(^4S)$	
State	Weight	State	Weight
$^2\Sigma^+_{g(u)}$	2	$^4\Sigma^-_{g(u)}$	4
$^2\Pi_{g(u)}$	4	$^4\Pi_{g(u)}$	8
$^4\Sigma^+_{g(u)}$	4	$^4\Delta_{g(u)}$	8
$^4\Pi_{g(u)}$	8		
$^6\Sigma^+_{g(u)}$	6		
$^6\Pi_{g(u)}$	12		

the colliding particle pair. The partial resonance charge exchange cross sections of a pair of symmetrical g and antisymmetric u molecular states with the same spin S and angular momentum Λ can be expressed by the following formula:[18]

$$Q^{2S+1}_{ex,\Lambda}(E) = \frac{\pi}{k^2}\sum_{l=0}^{\infty}(2l+1)\sin^2(\eta_l^g - \eta_l^u) \quad (5)$$

where l is the angular momentum quantum number, k is the wave number, and η_l^g and η_l^u are phase shifts for the symmetric and antisymmetric states, respectively, which can be defined by the semi-classical Wentzel–Kramers–Brillouin (WKB) approximation[18]

$$\eta_l = k\left\{\int_{r_x}^{\infty}[G(r)]^{1/2}dr - \int_b^{\infty}\left[1-\left(\frac{l+1}{kr}\right)^2\right]^{1/2}dr\right\} \quad (6)$$

where r_x is the lower limit of the integral, which is largest root of the following equation

$$G(r) \equiv 1 - \frac{V(r)}{E} - \frac{b^2}{r^2} = 0 \quad (7)$$

where $V(E)$ is the PEC, and the impact parameter b is equal to $(l+1/2)/k$. The relationship between the mean inelastic cross section and the resonance charge exchange cross section is as follows

$$\tilde{Q}^{(n)}_{in}(E) = 2Q_{ex}(E) \quad (8)$$

where n is odd. Moreover, Dalgarno *et al.*[28] pointed out that this relationship is probably valid for temperatures greater than 400 K in most cases.

For the elastic collision, the momentum transfer, viscosity, and third moment cross sections can be calculated using the following equation[29,30]

$$Q^{(n)}_{el}(E) = \frac{4\pi}{k^2}\sum_{v}^{n}\sum_{l=0}^{\infty}a^l_{nv}\sin^2(\eta_{l+v} - \eta_l) \quad (9)$$

where the values of v are odd or even according to the odd or even parity of n. The coefficients a^l_{nv} can be determined by recursion from ref. 18 and 31

$$(2l+1)x^n P_l(x) = \sum_{\nu=-n}^{n}a^l_{n\nu}P_{l+\nu}(x) \quad (10)$$

where $P_l(x)$ is the Legendre polynomial. The inelastic and elastic cross sections are obtained by the weighted average of electronic states,[17,18] and the weighting factors are listed in Table 1.

In this work, we calculated the inelastic and elastic cross sections in the energy range of 10^{-6} to 10 Hartree. To ensure precision, we extended the angular momentum quantum number l to 30 000 for resonance charge exchange calculations and 10 000 for elastic cross sections, achieving a decimal accuracy of five significant figures in both cases.

3. Results and discussion

In this study, the *ab initio* calculations for $O(^3P)$–$O^+(^4S)$ and $O(^1D)$–$O^+(^4S)$ interactions were performed using the MOLPRO 2015 program package.[32,33] Our calculations employed the icMRCI + Q method,[34,35] and adopted the aug-cc-pwCV5Z-DK basis set to describe the oxygen atom and the oxygen ion. To enhance the accuracy of excited-state calculations, the active space included 2 closed orbitals and 14 active molecular orbitals. For the O_2^+ molecule, which belongs to the $D_{\infty h}$ symmetry, calculations were adapted to the D_{2h} point group because the MOLPRO 2015 program package only allows Abelian point-group symmetries. The reducing map of irreducible representations between $D_{\infty h}$ and D_{2h} follows: $\Sigma^+_g \rightarrow A_g$, $\Sigma^-_g \rightarrow B_{1g}$, $\Sigma^+_u \rightarrow B_{1u}$, $\Sigma^-_u \rightarrow A_u$, $\Pi_g \rightarrow (B_{2g}, B_{3g})$, $\Pi_u \rightarrow (B_{2u}, B_{3u})$, $\Delta_g \rightarrow (A_g, B_{1g})$, and $\Delta_u \rightarrow (B_{1u}, A_u)$.

The present PECs of O^+_2 obtained in this study are presented in Fig. 2. Eighteen electronic states correlating to the $O(^3P)$–$O^+(^4S)$ and $O(^1D)$–$O^+(^4S)$ dissociation limits were calculated, including X $^2\Pi_g$, A $^2\Pi_u$, B $^2\Sigma^+_u$, 1 $^2\Sigma^+_g$, 1 $^4\Sigma^+_g$, 1 $^4\Sigma^+_u$, 1 $^4\Pi_g$, a $^4\Pi_u$, 1 $^6\Sigma^+_g$, 1 $^6\Sigma^+_u$, 1 $^6\Pi_g$, 1 $^6\Pi_u$, 1 $^4\Sigma^-_g$, 1 $^4\Sigma^-_u$, 2 $^4\Pi_g$, b $^4\Pi_u$, 1 $^4\Delta_g$, and 1 $^4\Delta_u$ electronic states. However, *ab initio* methods have limitations in resolving potential energies at extremely short internuclear distances; thus, we extrapolated the potential energy points to 10^{-6} Å using an exponential form $V(r) = a + be^{-cr}$, where a, b, and c are the fitting parameters.[36] For the remaining regions, potential energy points were interpolated using a cubic spline algorithm implemented *via* the *scipy.interpolate.interp1d* module in Python,[37] ensuring smooth continuity for subsequent transport cross section calculations. Notably, the short internuclear distances have been demonstrated to affect the collision integrals at high temperatures.[22,25] Taking the collision integrals approaching 50 000 K for example, the average translational energy is approximately 6.5 eV. In order to obtain the collision integral accurately, the short range region of PECs needs to be extended to 30–50 eV energies.[24] However, PECs of existing studies only covered the low-energy range, potentially introducing deviations in high-temperature predictions. To address this gap, our calculations extend the potential energy points to a broader energy range (>1.38 Hartree), ensuring accuracy in transport cross sections and collision integrals in this work.

As illustrated in Fig. 3, the PECs for the $O(^3P)$–$O^+(^4S)$ interaction are compared with theoretical results from Knof

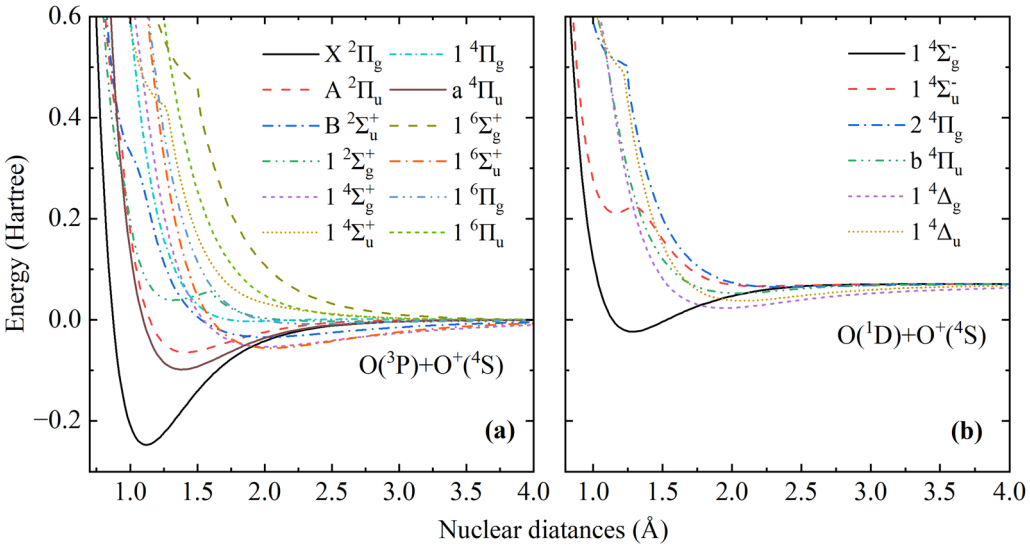

Fig. 2 Potential energy curves for the electronic states corresponding to (a) O(^{3}P)–O$^+$(^{4}S) and (b) O(^{1}D)–O$^+$(^{4}S) interactions.

et al.,[6] Stallcop *et al.*,[18] and Moss *et al.*[38] Knof *et al.*[6] derived their PECs from experimental spectroscopic data and extrapolated to the dissociation limit using the HH function, while Stallcop *et al.*[18] and Moss *et al.*[38] employed the CASSCF method. Our results are in agreement with previous studies, except for the 1 $^4\Sigma_g^+$ and 1 $^6\Sigma_u^+$ electronic states. For the 1 $^4\Sigma_g^+$ state, results of Stallcop *et al.*[18] and Moss *et al.*[38] showed a shoulder near 1.3 Å, a feature absent in our calculations. For the 1 $^6\Sigma_u^+$ state, our results and those of Moss *et al.*[38] are slightly higher than those of Stallcop *et al.*[18] within the 1.2–2.0 Å range. Overall, our *ab initio* PECs are reliable.

The resonance charge transfer is an important mechanism for determining the diffusion type of the transport property, which corresponds to the odd-order cross sections. Fig. 4 presents the resonance charge exchange cross sections for the O(^{3}P)–O$^+$(^{4}S) interaction. For comparison, the experimental results are from Stebbings *et al.*,[39] and the theoretical results are from Kosarim *et al.*,[40] Eletskii *et al.*,[9] Stallcop *et al.*,[18] Knof *et al.*,[6] and Rapp *et al.*[41] Generally, our calculated data are systematically higher than previous theoretical values, except for the results of Kosarim *et al.*[40] The WKB approximation, while reliable for high-energy collisions, does exhibit known limitations in the low-energy regime due to pronounced quantum effects. Our calculated cross sections exhibit pronounced oscillations induced by quantum effects at low collision energies, with such oscillations

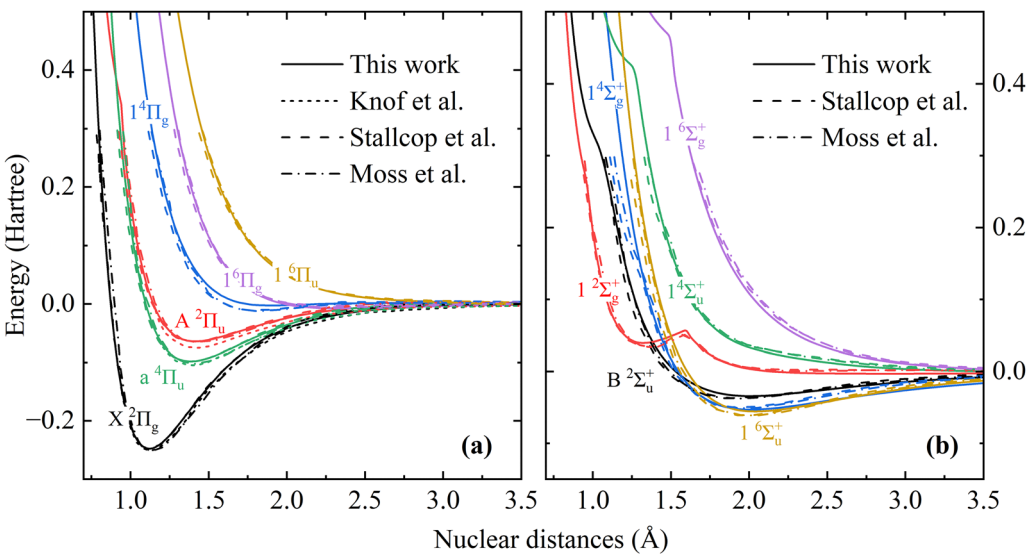

Fig. 3 Potential energy curves for the (a) Π and (b) Σ electronic states corresponding to the O(^{3}P)–O$^+$(^{4}S) interaction, where the solid lines are this results, and the theoretical results are from Knof *et al.*[6] (dot lines), Stallcop *et al.*[18] (dashed lines), and Moss *et al.*[38] (dot-dashed lines).

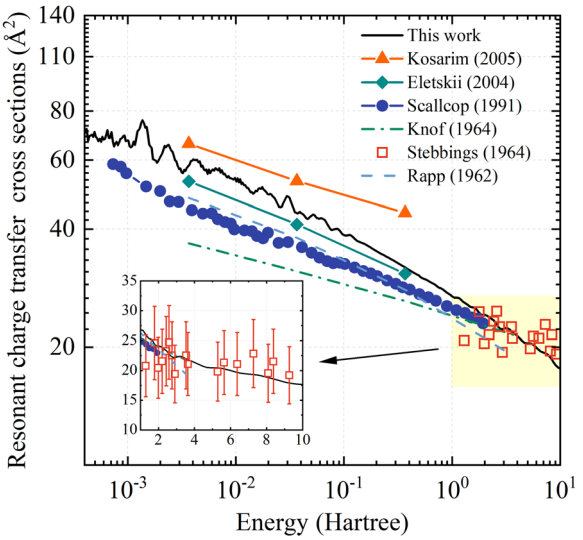

Fig. 4 Comparison of the resonance charge exchange cross sections for the $O(^3P)$–$O^+(^4S)$ interaction as a function of collision energy, where the experimental results are from Stebbings *et al.*[39] (squares), and the theoretical results are from Kosarim *et al.*[40] (triangles), Eletskii *et al.*[9] (rhombuses), Stallcop *et al.*[18] (cycles), Knof *et al.*[6] (dot-dashed line), and Rapp *et al.*[41] (dashed line), respectively.

diminishing significantly at around 0.1 Hartree, which may introduce certain uncertainties to the results within this energy range. Compared to those of Stallcop *et al.*,[18] our results show an average deviation of 21% below 0.1 Hartree, which gradually decreases as the impact energy increases. Compared with the results calculated by Knof *et al.*[6] based on the semi-empirical method, the deviation reaches a maximum of 36.5% at 0.1 eV. The difference is mainly due to the deviation brought by the semi-empirical method. The subgraph in Fig. 4 presents a detailed comparison between our results and the experimental data from Stebbings *et al.*[39] in the energy range of 1 to 10 Hartree. The experimental measurements have an estimated uncertainty of ±25%. As shown in the figure, our resonance charge transfer cross sections fall within the bounds of this experimental uncertainty.

Fig. 5 illustrates the mean transport cross sections $\bar{Q}_{in}^{(1)}$ (inelastic) and $\bar{Q}_{el}^{(2)}$ (elastic) for the $O(^3P)$–$O^+(^4S)$ interaction. Stallcop *et al.*[18] accounted for the nuclear spin effect at low collision energies and evaluated the contributions of each gerade and ungerade pairs to the transport cross sections at different energies. In contrast, many studies[11,27,42] determined the inelastic cross sections by using twice the resonance charge transfer cross sections over the entire collision energy range. For electronic state weighting, the general treatment is that the statistical weight is equal to the spin multipotential interaction of the Σ state and is equal to twice the spin multipotential interaction of the Π and Δ states.[17,24] As with the treatment for calculating transport cross sections for the N–N^+ interaction,[11] we adopted these common treatments of most previous studies in this work, with detailed weighting factors tabulated in Table 1. Our inelastic cross sections are systematically 4–27% higher than those of Stallcop *et al.*[18] In contrast, viscosity cross sections are in satisfactory agreement (<3% deviation), suggesting that viscosity-dominated transport properties may be less sensitive to PEC details than resonance charge transfer processes.

Table 2 presents the diffusion- and viscosity-type collision integrals, $\sigma^2\Omega^{(1,1)*}$ and $\sigma^2\Omega^{(2,2)*}$, for the $X\ ^2\Pi_g$, $A\ ^2\Pi_u$, and $1\ ^2\Sigma_u^+$ states. These states represent the bound state, repulsive state, and state with a complex structure, respectively, as shown in Fig. 1. For comparison, results derived from the Morse functions (for bound states) and exponential functions (for repulsive states) are included. The functional forms are as follows:

$$V(r) = D_e\left\{\exp\left[-\frac{2C}{\sigma}(r-r_e)\right] - 2\exp\left[-\frac{C}{\sigma}(r-r_e)\right]\right\} \quad (11)$$

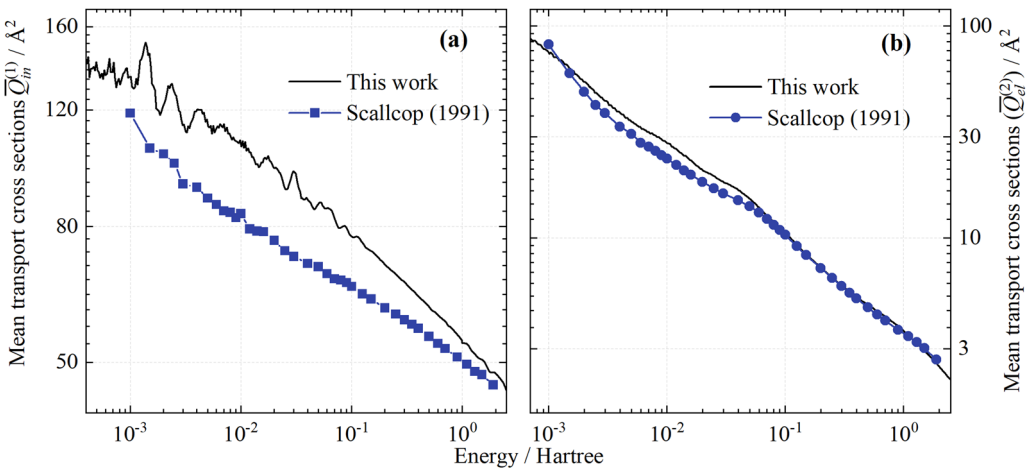

Fig. 5 Comparison of the mean transport cross sections (a) $\bar{Q}_{in}^{(1)}$ and (b) $\bar{Q}_{el}^{(2)}$ for the $O(^3P)$–$O^+(^4S)$ interaction, where the square and cycle symbols are from Stallcop *et al.*[18]

Table 2 Comparison of diffusion- and viscosity-type collision integrals $\sigma^2\Omega^{(1,1)*}$ and $\sigma^2\Omega^{(2,2)*}$ (in Å^2) for the X $^2\Pi_g$, A $^2\Pi_u$, and 1 $^4\Sigma_u^+$ states between the present results (columns a) and those of Laricchiuta *et al.*[19] (columns b)

	X $^2\Pi_g$		A $^2\Pi_u$		1 $^4\Sigma_u^+$	
T/K	$(1,1)^a$	$(1,1)^b$	$(1,1)^a$	$(1,1)^b$	$(1,1)^a$	$(1,1)^b$
500	11.48	11.47	8.06	11.49	15.99	4.23
1000	10.34	10.27	7.47	10.14	10.26	3.69
3000	8.18	8.49	6.22	7.87	6.00	2.91
5000	7.13	7.65	5.24	6.66	4.75	2.58
10 000	5.67	6.45	3.50	4.67	3.50	2.16
20 000	3.97	3.97	2.11	2.10	2.65	1.58
50 000	1.90	2.83	1.17	1.50	1.82	1.34

	X $^2\Pi_g$		A $^2\Pi_u$		1 $^4\Sigma_u^+$	
T/K	$(2,2)^a$	$(2,2)^b$	$(2,2)^a$	$(2,2)^b$	$(2,2)^a$	$(2,2)^b$
500	16.52	11.48	11.63	11.49	18.11	4.23
1000	14.61	10.27	10.77	10.14	12.55	3.69
3000	11.25	8.49	8.55	7.87	7.62	2.91
5000	9.66	7.64	6.7	6.66	6.04	2.58
10 000	7.4	6.45	4.04	4.66	4.51	2.16
20 000	4.65	3.97	2.4	2.10	3.47	1.58
50 000	2.01	2.83	1.43	1.50	2.29	1.34

where D_e is the potential well, r_e is the equilibrium internuclear distance, σ is the distance at which the potential crosses zero, and C is the potential parameter.

$$V(r) = A\exp(-\alpha r) \quad (12)$$

where A and α are the potential parameters. The parameters for these states were adopted from Laricchiuta *et al.*[19] As shown in Table 2, our *ab initio* results are in good agreement with Morse-based predictions for bound states but exhibit significant deviations for repulsive states and states with complex PECs. Notably, the results of the 1 $^2\Sigma_u^+$ state show a maximum deviation of 73% at 500 K, primarily due to the inability of analytical potentials to capture the intricate details of the O(^{3}P)–O$^+$(^{4}S) interaction, especially for PECs with complex structures.

Table 3 compares the diffusion- and viscosity-type collision integrals $\sigma^2\Omega^{(1,1)*}$ and $\sigma^2\Omega^{(2,2)*}$ for the O(^{3}P)–O$^+$(^{4}S) interaction. For comparison, the results of Stallcop *et al.*,[18]

Table 3 Comparison between collision integrals $\sigma^2\Omega^{(1,1)*}$ and $\sigma^2\Omega^{(2,2)*}$ (in Å^2) for the O(^{3}P)–O$^+$(^{4}S) interaction calculated in the present work (columns a), Stallcop *et al.*[18] (columns b), Capitelli *et al.*[43] (columns c) and Capitelli *et al.*[17] (columns d), and Laricchiuta *et al.*[19] (columns e)

T/K	$(1,1)^a$	$(1,1)^b$	$(1,1)^d$	$(1,1)^e$	$(2,2)^a$	$(2,2)^b$	$(2,2)^c$	$(2,2)^d$	$(2,2)^e$
500	40.97	29.64	28.88	—	16.97	14.78	15.22	10.26	—
2000	33.35	24.88	25.49	34.60	9.93	8.72	6.50	7.30	7.74
5000	29.01	22.60	23.36	—	6.87	6.39	4.74	5.49	—
10 000	26.08	21.13	21.82	31.846	4.89	4.75	4.02	4.27	4.67
15 000	24.29	20.30	20.94	—	3.96	3.92	3.67	3.64	—
20 000	23.42	19.72	20.33	29.840	3.43	3.41	3.45	3.23	3.47
30 000	21.96	18.90	19.48	—	2.82	2.81	—	2.71	—
50 000	20.22	17.19	18.43	—	2.24	2.23	—	2.15	—

Table 4 Comparison between collision integrals $\sigma^2\Omega^{(1,1)*}$ and $\sigma^2\Omega^{(2,2)*}$ (in Å^2) for the O(^{1}D)–O$^+$(^{4}S) interaction calculated in the present work (columns a), and Laricchiuta *et al.*[19] (columns b)

T/K	$(1,1)^a$	$(1,1)^b$	$(2,2)^a$	$(2,2)^b$
2000	11.21	8.81	11.49	8.95
4000	7.31	6.74	8.04	7.11
6000	5.54	5.56	6.26	6.03
8000	4.54	4.77	5.20	5.29
10 000	3.91	4.19	4.51	4.73
12 000	3.48	3.76	4.04	4.29
16 000	2.92	3.13	3.42	3.65
20 000	2.57	2.69	3.03	3.18

Capitelli *et al.*,[43] Capitelli *et al.*,[17] and Laricchiuta *et al.*[19] are also included. Capitelli *et al.*[17] did not consider the contribution of elastic collision. For inelastic collision integrals, deviations between our calculations and those of Stallcop *et al.*,[18] and Capitelli *et al.*[17] range from 13.2% to 29.5%, which gradually decreases with the increase in temperature. The collision integral of Laricchiuta *et al.*[19] at 15 000 and 200 000 K is significantly higher. While the temperature is up to 50 000 K, the deviation with Capitelli *et al.*[17] decreases to 10.8%. In contrast, our viscosity collision integrals show excellent agreement with those of Stallcop *et al.*,[18] with a maximum deviation of only 2.6% between 15 000 and 50 000 K. Notably, the results of analytic potentials[17,19,43] deviate significantly from the *ab initio* results, especially at low temperatures, which emphasizes the necessity of employing *ab initio* methods for accurate collision integral predictions.

Table 4 presents the elastic and viscosity collision integrals for the O(^{1}D)–O$^+$(^{4}S) interaction. Laricchiuta *et al.*[19] provided the elastic collision integrals $\sigma^2\Omega^{(1,1)*}$ and the viscosity collision

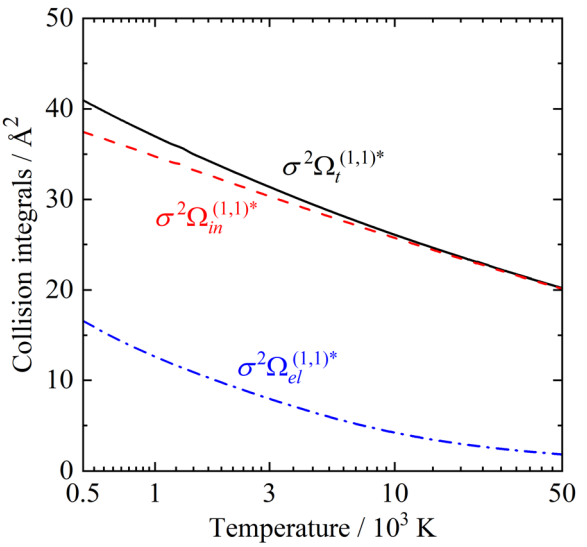

Fig. 6 The total collision integrals (solid line) corresponding to the O(^{3}P)–O$^+$(^{4}S) interaction, resulting from elastic (dashed line) and resonance charge exchange (dot-dashed line) contributions.

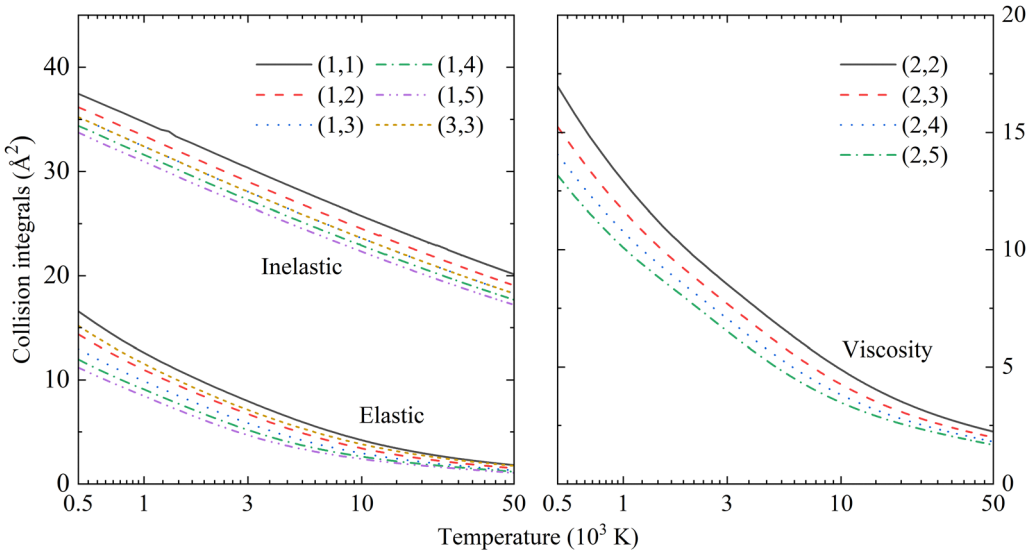

Fig. 7 The inelastic, elastic and viscosity collision integrals corresponding to the O(^{3}P)–O$^+$(^{4}S) interaction as a function of temperatures.

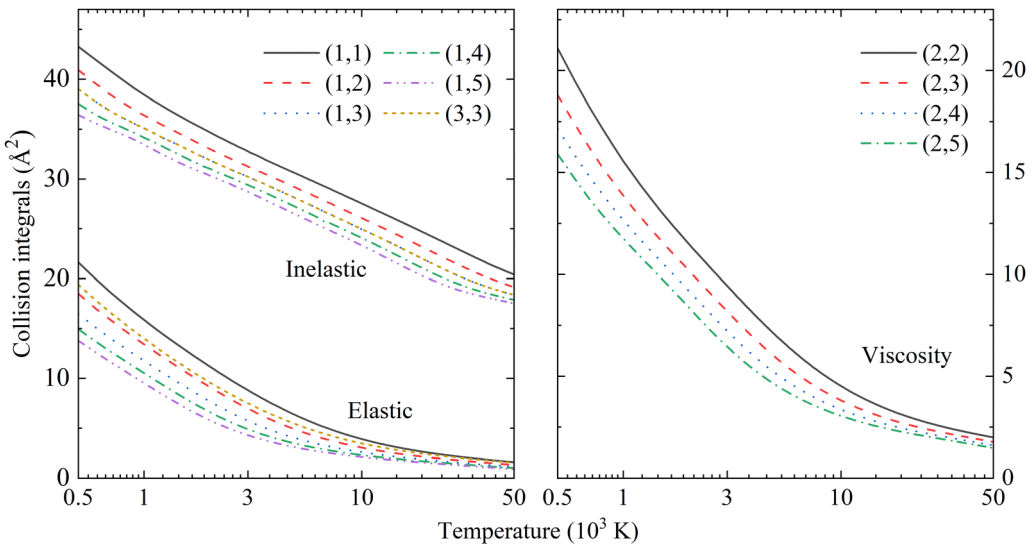

Fig. 8 The inelastic, elastic and viscosity collision integrals corresponding to the O(^{3}P)–O$^+$(^{4}S) and interaction as a function of temperatures.

integrals $\sigma^2\Omega^{(2,2)*}$ based on the analytical potential energy functions. Compared to their results, our calculations exhibit a significant deviation of 22% at low temperatures (<6000 K), which diminishes to less than 8% above 6000 K. The deviation of our results from the collision integrals for the O(^{1}D)–O$^+$(^{4}S) interaction is significantly smaller than that for the O(^{3}P)–O$^+$(^{4}S) interaction. This discrepancy arises because the PECs for the O(^{1}D)–O$^+$(^{4}S) interaction are predominantly Morse or repulsive potentials, which can be accurately reproduced by the analytic potentials.

Fig. 6 illustrates the contribution of elastic and inelastic collision integrals for the total collision integrals for the O(^{3}P)–O$^+$(^{4}S) interaction. At 500 K, the inelastic collision process contributes a maximum of ~84.6% to the total collision integral. Despite resonance charge exchange processes being predominant, the contribution of elastic collisions remains non-negligible, particularly for accurate transport property calculations at lower temperatures. The elastic collision still contributes 3% at temperatures up to 8500 K.

Fig. 7–9 present the inelastic, elastic, viscosity and total collision integrals for O(^{3}P)–O$^+$(^{4}S) and O(^{1}D)–O$^+$(^{4}S) interactions. The reported collision integrals included $\Omega^{(1,1)*}$, $\Omega^{(1,2)*}$, $\Omega^{(1,3)*}$, $\Omega^{(1,4)*}$, $\Omega^{(1,5)*}$, $\Omega^{(2,2)*}$, $\Omega^{(2,3)*}$, $\Omega^{(2,4)*}$, $\Omega^{(2,5)*}$, and $\Omega^{(3,3)*}$.

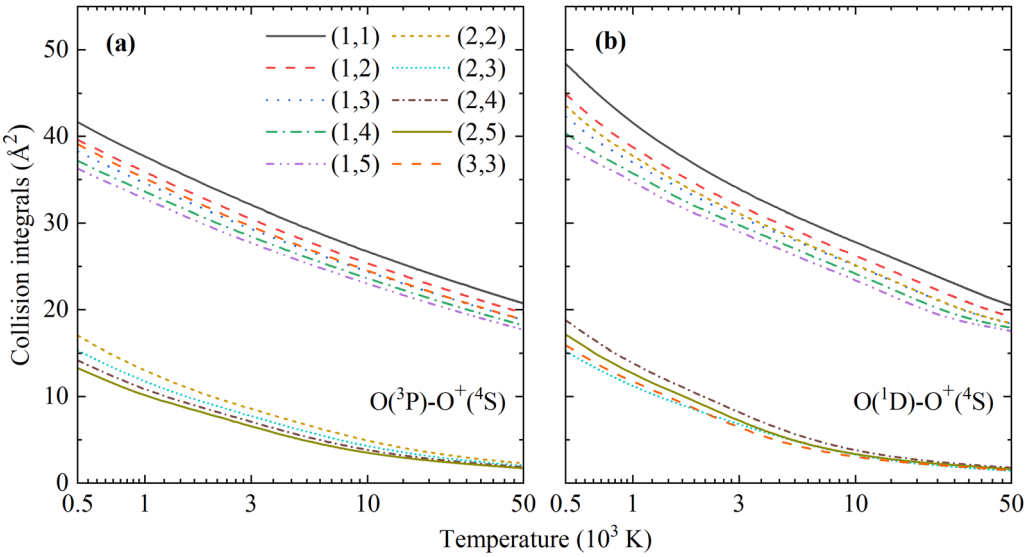

Fig. 9 The total collision integrals corresponding to (a) $O(^3P)$–$O^+(^4S)$ and (b) $O(^1D)$–$O^+(^4S)$ interactions as a function of temperatures.

For more detailed data, refer to the SI. Moreover, we provide the fitting functions of collision integrals, and the formula is as follows:

$$f_{\sigma^2\Omega^{(l,s)*}}(T) = a_1 + a_2T + a_3T^2 + a_4T^3 + a_5T^4 + \frac{b_1}{T} + \frac{b_2}{T^2} \quad (13)$$

where a_1, a_2, a_3, a_4, a_5, b_1, and b_2 are the fitting parameters. In the Appendix, Tables 5–10 present the fitting parameters of inelastic, elastic and total collision integrals for $O(^3P)$–$O^+(^4S)$ and $O(^1D)$–$O^+(^4S)$ interactions. The average fitting errors of all collision integrals do not exceed 1.8%.

4. Conclusions

In the present work, a complete set of inelastic, elastic and total collision integrals for $O(^3P)$–$O^+(^4S)$ and $O(^1D)$–$O^+(^4S)$ interactions in the temperature range of 500–50 000 K have been derived in the framework of the semi-classical method. The high-quality *ab initio* potential energy points are computed based on the aug-cc-pWCV5Z-DK basis set, with an extended energy range to ensure the accuracy of transport cross sections and collision integrals. The collision integrals involving the electronic excited state improve the scarce and incomplete results in the literature and further complement the particle collision database in air plasma. The resonance charge exchange cross sections obtained by using the high-level *ab initio* method are compared with the existing experimental data, and a good agreement is obtained. This work also evaluates the contributions of elastic and inelastic processes. Inelastic collision processes contribute more than 85% of the total value at low temperatures, but elastic collision processes cannot be ignored for odd-order collision interactions. The calculated data in this work are helpful for the establishment of a high-precision re-entry model for oxygen-containing plasmas.

Author contributions

Zi Ding: formal analysis (equal), investigation (equal), funding acquisition (equal), methodology (equal), software (equal), and writing – original draft (equal). Linhua Liu: conceptualization (lead), supervision (lead), funding acquisition (equal), and writing – review and editing (equal).

Conflicts of interest

There are no conflicts of interest.

Data availability

The data supporting this article have been included as part of the SI.

The SI includes the *ab initio* potential energy points for $O(^3P)$–$O^+(^4S)$ and $O(^1D)$–$O^+(^4S)$ interactions given in $O(^3P)$–$O^+(^4S)$ potential energy points.txt, $O(^1D)$–$O^+(^4S)$ potential energy points.txt. The inelastic, elastic, and total collision integrals for $O(^3P)$–$O^+(^4S)$ and $O(^1D)$–$O^+(^4S)$ interactions given in $O(^3P)$–$O^+(^4S)$ elastic collision integrals.txt, $O(^3P)$–$O^+(^4S)$ inelastic collision integrals.txt, $O(^3P)$–$O^+(^4S)$ total collision integrals.txt, $O(^1D)$–$O^+(^4S)$ elastic collision integrals.txt, $O(^1D)$–$O^+(^4S)$ inelastic collision integrals.txt and $O(^1D)$–$O^+(^4S)$ total collision integrals.txt. See DOI:**https://doi.org/10.1039/d5cp01234a**

Appendix

The parameters for fitting functions of collision integrals

Table 5 Parameters used to fit the inelastic collision integrals for the $O(^3P)-O^+(^4S)$ interaction

$\Omega^{(i,j)*}$	a_1	a_2	a_3	a_4	a_5	b_1	b_2	b_3
(1,1)	2.963×10^{1}	-6.549×10^{-4}	2.331×10^{-8}	-4.452×10^{-13}	3.287×10^{-18}	7.848×10^{3}	-1.962×10^{6}	2.963×10^{1}
(1,2)	2.827×10^{1}	-6.323×10^{-4}	2.221×10^{-8}	-4.186×10^{-13}	3.057×10^{-18}	7.796×10^{3}	-1.917×10^{6}	2.827×10^{1}
(1,3)	2.731×10^{1}	-6.229×10^{-4}	2.192×10^{-8}	-4.127×10^{-13}	3.011×10^{-18}	7.680×10^{3}	-1.854×10^{6}	2.731×10^{1}
(1,4)	2.653×10^{1}	-6.120×10^{-4}	2.148×10^{-8}	-4.027×10^{-13}	2.926×10^{-18}	7.616×10^{3}	-1.838×10^{6}	2.653×10^{1}
(1,5)	2.593×10^{1}	-6.091×10^{-4}	2.151×10^{-8}	-4.039×10^{-13}	2.936×10^{-18}	7.492×10^{3}	-1.786×10^{6}	2.593×10^{1}
(3,3)	2.731×10^{1}	-6.229×10^{-4}	2.192×10^{-8}	-4.127×10^{-13}	3.011×10^{-18}	7.680×10^{3}	-1.854×10^{6}	2.731×10^{1}

Table 6 Parameters used to fit the elastic collision integrals for the $O(^3P)-O^+(^4S)$ interaction

$\Omega^{(i,j)*}$	a_1	a_2	a_3	a_4	a_5	b_1	b_2	b_3
(1,1)	6.500×10^{0}	-4.776×10^{-4}	2.101×10^{-8}	-4.320×10^{-13}	3.290×10^{-18}	8.432×10^{3}	-1.712×10^{6}	6.500×10^{0}
(1,2)	5.072×10^{0}	-3.838×10^{-4}	1.761×10^{-8}	-3.722×10^{-13}	2.886×10^{-18}	8.273×10^{3}	-1.847×10^{6}	5.072×10^{0}
(1,3)	3.988×10^{0}	-2.914×10^{-4}	1.360×10^{-8}	-2.926×10^{-13}	2.296×10^{-18}	8.262×10^{3}	-1.935×10^{6}	3.988×10^{0}
(1,4)	3.193×10^{0}	-2.144×10^{-4}	9.989×10^{-9}	-2.169×10^{-13}	1.716×10^{-18}	8.157×10^{3}	-1.937×10^{6}	3.193×10^{0}
(1,5)	2.615×10^{0}	-1.544×10^{-4}	7.016×10^{-9}	-1.528×10^{-13}	1.216×10^{-18}	7.961×10^{3}	-1.887×10^{6}	2.615×10^{0}
(3,3)	5.472×10^{0}	-3.768×10^{-4}	1.649×10^{-8}	-3.390×10^{-13}	2.582×10^{-18}	8.310×10^{3}	-1.749×10^{6}	5.472×10^{0}

Table 7 Parameters used to fit the total collision integrals for the $O(^3P)-O^+(^4S)$ interaction

$\Omega^{(i,j)*}$	a_1	a_2	a_3	a_4	a_5	b_1	b_2	b_3
(1,1)	3.010×10^{1}	-7.105×10^{-4}	2.612×10^{-8}	-5.069×10^{-13}	3.775×10^{-18}	1.001×10^{4}	-2.293×10^{6}	3.010×10^{1}
(1,2)	2.850×10^{1}	-6.634×10^{-4}	2.391×10^{-8}	-4.577×10^{-13}	3.375×10^{-18}	9.720×10^{3}	-2.260×10^{6}	2.850×10^{1}
(1,3)	2.738×10^{1}	-6.354×10^{-4}	2.271×10^{-8}	-4.321×10^{-13}	3.175×10^{-18}	9.443×10^{3}	-2.188×10^{6}	2.738×10^{1}
(1,4)	2.651×10^{1}	-6.123×10^{-4}	2.163×10^{-8}	-4.076×10^{-13}	2.974×10^{-18}	9.227×10^{3}	-2.143×10^{6}	2.651×10^{1}
(1,5)	2.586×10^{1}	-6.014×10^{-4}	2.121×10^{-8}	-3.986×10^{-13}	2.901×10^{-18}	8.964×10^{3}	-2.062×10^{6}	2.586×10^{1}
(2,2)	7.550×10^{0}	-5.040×10^{-4}	2.104×10^{-8}	-4.170×10^{-13}	3.096×10^{-18}	7.108×10^{3}	-1.177×10^{6}	7.550×10^{0}
(2,3)	6.763×10^{0}	-4.858×10^{-4}	2.141×10^{-8}	-4.393×10^{-13}	3.334×10^{-18}	6.722×10^{3}	-1.233×10^{6}	6.763×10^{0}
(2,4)	6.022×10^{0}	-4.471×10^{-4}	2.042×10^{-8}	-4.293×10^{-13}	3.310×10^{-18}	6.686×10^{3}	-1.344×10^{6}	6.022×10^{0}
(2,5)	5.333×10^{0}	-3.971×10^{-4}	1.855×10^{-8}	-3.967×10^{-13}	3.094×10^{-18}	6.814×10^{3}	-1.481×10^{6}	5.333×10^{0}
(3,3)	2.763×10^{1}	-6.586×10^{-4}	2.373×10^{-8}	-4.524×10^{-13}	3.325×10^{-18}	9.748×10^{3}	-2.192×10^{6}	2.763×10^{1}

Table 8 Parameters used to fit the inelastic collision integrals for the $O(^1D)-O^+(^4S)$ interaction

$\Omega^{(i,j)*}$	a_1	a_2	a_3	a_4	a_5	b_1	b_2	b_3
(1,1)	3.17×10^{1}	-6.79×10^{-4}	2.12×10^{-8}	-3.82×10^{-13}	2.78×10^{-18}	9.21×10^{3}	-1.68×10^{6}	3.17×10^{1}
(1,2)	3.07×10^{1}	-7.24×10^{-4}	2.24×10^{-8}	-3.89×10^{-13}	2.78×10^{-18}	7.86×10^{3}	-1.35×10^{6}	3.07×10^{1}
(1,3)	2.98×10^{1}	-7.44×10^{-4}	2.24×10^{-8}	-3.65×10^{-13}	2.46×10^{-18}	7.56×10^{3}	-1.47×10^{6}	2.98×10^{1}
(1,4)	2.90×10^{1}	-7.56×10^{-4}	2.21×10^{-8}	-3.29×10^{-13}	1.98×10^{-18}	7.62×10^{3}	-1.67×10^{6}	2.90×10^{1}
(1,5)	2.85×10^{1}	-7.96×10^{-4}	2.40×10^{-8}	-3.47×10^{-13}	1.92×10^{-18}	7.47×10^{3}	-1.70×10^{6}	2.85×10^{1}
(3,3)	2.98×10^{1}	-7.44×10^{-4}	2.24×10^{-8}	-3.65×10^{-13}	2.46×10^{-18}	7.56×10^{3}	-1.47×10^{6}	2.98×10^{1}

Table 9 Parameters used to fit the elastic collision integrals for the $O(^1D)-O^+(^4S)$ interaction

$\Omega^{(i,j)*}$	a_1	a_2	a_3	a_4	a_5	b_1	b_2	b_3
(1,1)	5.54×10^{0}	-4.86×10^{-4}	2.36×10^{-8}	-5.13×10^{-13}	4.04×10^{-18}	1.42×10^{4}	-3.15×10^{6}	5.54×10^{0}
(1,2)	3.34×10^{0}	-2.68×10^{-4}	1.37×10^{-8}	-3.10×10^{-13}	2.51×10^{-18}	1.37×10^{4}	-3.16×10^{6}	3.34×10^{0}
(1,3)	1.99×10^{0}	-1.12×10^{-4}	5.89×10^{-9}	-1.40×10^{-13}	1.18×10^{-18}	1.30×10^{4}	-2.97×10^{6}	1.99×10^{0}
(1,4)	1.24×10^{0}	-1.57×10^{-5}	7.22×10^{-10}	-2.40×10^{-14}	2.45×10^{-19}	1.20×10^{4}	-2.64×10^{6}	1.24×10^{0}
(1,5)	8.67×10^{-1}	3.59×10^{-5}	-2.27×10^{-9}	4.57×10^{-14}	-3.24×10^{-19}	1.08×10^{4}	-2.23×10^{6}	8.67×10^{-1}
(3,3)	4.18×10^{0}	-3.20×10^{-4}	1.55×10^{-8}	-3.38×10^{-13}	2.67×10^{-18}	1.31×10^{4}	-2.81×10^{6}	4.18×10^{0}

Table 10 Parameters used to fit the collision integrals for the $O(^1D)$–$O^+(^4S)$ interaction

$\Omega^{(i,j)*}$	a_1	a_2	a_3	a_4	a_5	b_1	b_2	b_3
(1,1)	3.16×10^{1}	-6.91×10^{-4}	2.23×10^{-8}	-4.13×10^{-13}	3.06×10^{-18}	1.32×10^{4}	-2.41×10^{6}	3.16×10^{1}
(1,2)	3.04×10^{1}	-6.95×10^{-4}	2.13×10^{-8}	-3.72×10^{-13}	2.66×10^{-18}	1.12×10^{4}	-1.96×10^{6}	3.04×10^{1}
(1,3)	2.94×10^{1}	-6.99×10^{-4}	2.03×10^{-8}	-3.23×10^{-13}	2.15×10^{-18}	1.03×10^{4}	-1.91×10^{6}	2.94×10^{1}
(1,4)	2.86×10^{1}	-7.08×10^{-4}	1.98×10^{-8}	-2.80×10^{-13}	1.60×10^{-18}	9.84×10^{3}	-1.96×10^{6}	2.86×10^{1}
(1,5)	2.81×10^{1}	-7.52×10^{-4}	2.18×10^{-8}	-2.99×10^{-13}	1.54×10^{-18}	9.25×10^{3}	-1.87×10^{6}	2.81×10^{1}
(2,2)	7.42×10^{0}	-6.35×10^{-4}	3.00×10^{-8}	-6.38×10^{-13}	4.95×10^{-18}	1.12×10^{4}	-2.20×10^{6}	7.42×10^{0}
(2,3)	5.84×10^{0}	-5.08×10^{-4}	2.52×10^{-8}	-5.51×10^{-13}	4.36×10^{-18}	1.13×10^{4}	-2.45×10^{6}	5.84×10^{0}
(2,4)	4.50×10^{0}	-3.75×10^{-4}	1.92×10^{-8}	-4.31×10^{-13}	3.46×10^{-18}	1.15×10^{4}	-2.68×10^{6}	4.50×10^{0}
(2,5)	3.45×10^{0}	-2.59×10^{-4}	1.36×10^{-8}	-3.13×10^{-13}	2.55×10^{-18}	1.16×10^{4}	-2.81×10^{6}	3.45×10^{0}
(3,3)	2.96×10^{1}	-7.29×10^{-4}	2.19×10^{-8}	-3.60×10^{-13}	2.44×10^{-18}	1.10×10^{4}	-2.01×10^{6}	2.96×10^{1}

Acknowledgements

This work is supported by the National Natural Science Foundation of China (52076123) and the Young Student Basic Research Project Training Program of Shandong University.

Notes and references

1 J. M. Yos, *Research and Advanced Development Division AVCO Corporation, Memorandum*, 1963, vol. 63.
2 J. G. Kim and S. M. Jo, *Int. J. Heat Mass Transfer*, 2021, **169**, 120950.
3 J. G. Kim, S. H. Kang and S. H. Park, *Int. J. Heat Mass Transfer*, 2020, **148**, 119059.
4 E. Farbar, I. D. Boyd and A. Martin, *J. Thermophys. Heat Transfer*, 2013, **27**, 593–606.
5 W. D. Pesnell, K. Omidvar and W. R. Hoegy, *Geophys. Res. Lett.*, 1993, **20**, 1343–1346.
6 H. Knof, E. Mason and J. Vanderslice, *J. Chem. Phys.*, 1964, **40**, 3548–3553.
7 H. Carlson and R. Harper, *J. Geophys. Res.*, 1977, **82**, 1144–1148.
8 P. Zhang, A. Dalgarno, R. Côté and E. Bodo, *Phys. Chem. Chem. Phys.*, 2011, **13**, 19026–19035.
9 A. Eletskii, M. Capitelli, R. Celiberto and A. Laricchiuta, *Phys. Rev. A: At., Mol., Opt. Phys.*, 2004, **69**, 042718.
10 J. R. Stallcop and H. Partridge, *Phys. Rev. A: At., Mol., Opt. Phys.*, 1985, **32**, 639.
11 Z. Ding, Z. Qin, M. Buchowiecki and L. Liu, *Phys. Fluids*, 2023, **35**, 087120.
12 J. O. Hirschfelder, C. F. Curtiss and R. B. Bird, *Molecular theory of gases and liquids*, 1964.
13 S. Chapman and T. G. Cowling, *The mathematical theory of non-uniform gases: an account of the kinetic theory of viscosity, thermal conduction and diffusion in gases*, Cambridge University Press, 1990.
14 J. R. Stallcop, H. Partridge and E. Levin, *Phys. Rev. A: At., Mol., Opt. Phys.*, 2001, **64**, 042722.
15 P. S. Krstić and D. R. Schultz, *Phys. Rev. A: At., Mol., Opt. Phys.*, 1999, **60**, 2118.
16 E. Levin and M. J. Wright, *J. Thermophys. Heat Transfer*, 2004, **18**, 143–147.
17 M. Capitelli, C. Gorse, S. Longo and D. Giordano, *J. Thermophys. Heat Transfer*, 2000, **14**, 259–268.
18 J. R. Stallcop, H. Partridge and E. Levin, *J. Chem. Phys.*, 1991, **95**, 6429–6439.
19 A. Laricchiuta, D. Bruno, M. Capitelli, R. Celiberto, C. Gorse and G. Pintus, *Chem. Phys.*, 2008, **344**, 13–20.
20 M. Buchowiecki, *At. Data Nucl. Data Tables*, 2023, **151**, 101574.
21 W. Zhao, Q. Hong, C. Yang, Q. Sun and Y. Hu, *Plasma Sources Sci. Technol.*, 2023, **32**, 125002.
22 M. Buchowiecki and P. Szabó, *Plasma Sources Sci. Technol.*, 2022, **31**, 045010.
23 S. McArdle, S. Endo, A. Aspuru-Guzik, S. C. Benjamin and X. Yuan, *Rev. Mod. Phys.*, 2020, **92**, 015003.
24 Z. Ding, Z. Qin and L. Liu, *Phys. Fluids*, 2024, **36**, 037105.
25 Z. Ding, Z. Qin and L. Liu, *Phys. Fluids*, 2023, **35**, 027127.
26 E. Levin, D. W. Schwenke, J. R. Stallcop and H. Partridge, *Chem. Phys. Lett.*, 1994, **227**, 669–675.
27 A. B. Murphy, *Plasma Chem. Plasma Process.*, 1995, **15**, 279–307.
28 A. Dalgarno and D. R. Bates, *Philos. Trans. R. Soc., A*, 1958, **250**, 426–439.
29 G. Heiche and E. Mason, *J. Chem. Phys.*, 1970, **53**, 4687–4696.
30 F. Meeks, T. Cleland, K. Hutchinson and W. Taylor, *J. Chem. Phys.*, 1994, **100**, 3813–3820.
31 E. Levin, H. Partridge and J. R. Stallcop, *J. Thermophys. Heat Transfer*, 1990, **4**, 469–477.
32 H. Werner, P. Knowles, G. Knizia, F. Manby, M. Schütz, P. Celani, W. Györffy, D. Kats, T. Korona and R. Lindh, *MOLPRO, version 2015.1, a package of ab initio programs*, University of Cardiff Chemistry Consultants (UC3), Cardiff, Wales, UK, 2015.
33 H. J. Werner, P. J. Knowles, G. Knizia, F. R. Manby and M. Schütz, *Wiley Interdiscip. Rev.: Comput. Mol. Sci.*, 2012, **2**, 242–253.
34 H. J. Werner and P. J. Knowles, *J. Chem. Phys.*, 1988, **89**, 5803–5814.
35 P. J. Knowles and H.-J. Werner, *Chem. Phys. Lett.*, 1988, **145**, 514–522.
36 R. J. Le Roy, *J. Quant. Spectrosc. Radiat. Transfer*, 2017, **186**, 167–178.
37 P. Virtanen, R. Gommers, T. E. Oliphant, M. Haberland, T. Reddy, D. Cournapeau, E. Burovski, P. Peterson, W. Weckesser and J. Bright, *Nat. Methods*, 2020, **17**, 261–272.

38 J. N. Moss and C. D. Scott, *Thermophysical aspects of re-entry flows*, American Institute of Aeronautics and Astronautics, 1986.
39 R. Stebbings, A. Smith and H. Ehrhardt, *J. Geophys. Res.*, 1964, **69**, 2349–2355.
40 A. Kosarim and B. Smirnov, *J. Exp. Theor. Phys.*, 2005, **101**, 611–627.
41 D. Rapp and W. E. Francis, *J. Chem. Phys.*, 1962, **37**, 2631–2645.
42 G. D. Dhamale, S. Nath, V. L. Mathe and S. Ghorui, *Phys. Plasmas*, 2017, **24**, 063514.
43 M. Capitelli, D. Cappelletti, G. Colonna, C. Gorse, A. Laricchiuta, G. Liuti, S. Longo and F. Pirani, *Chem. Phys.*, 2007, **338**, 62–68.